processes

MDPI

Article

Strategies for Optimizing Shut-In Time: New Insights from Shale Long-Term Hydration Experiments

Bo Zeng [1], Enjia Dong [2], Zhiguang Yao [1], Yi Song [1], Zhuang Xiong [2], Yongzhi Huang [1], Xiaoyan Gou [2] and Xiaodong Hu [2,*]

[1] PetroChina Southwest Oil & Gasfield Company, Chengdu 610017, China; zeng_bo@petrochina.com.cn (B.Z.); yaozg_2021@petrochina.com.cn (Z.Y.); sy09@petrochina.com.cn (Y.S.); huangyzhi@petrochina.com.cn (Y.H.)
[2] State Key Laboratory of Petroleum Resources and Engineering, China University of Petroleum, Beijing 102249, China; 2021216580@student.cup.edu.cn (E.D.); 2022211729@student.cup.edu.cn (Z.X.); 2021211849@student.cup.edu.cn (X.G.)
* Correspondence: huxiaodong@cup.edu.cn

Abstract: In the process of hydraulic fracturing, fracturing fluid invades the formation and reacts with shale. Water-sensitive clay minerals swell when exposed to water. This results in a change in the mechanical properties of shale. However, the influences of a long-term water–shale reaction on mechanical properties are still unclear, and an optimization strategy of the shut-in time is required. In this paper, an optimization strategy for the shut-in time based on a shale long-term hydration experiment is proposed. In this paper, the water–shale reaction is simulated by laboratory experiments under normal temperature and pressure. The experiments are performed based on specimens from a shale outcrop. Clay and mineral composition, Young's modulus, surface hardness, and tensile strength parameters are measured at 30-day intervals for 90 days. A CT scan was performed for 180 days. The experimental results show that the mass fraction of clay increased by 14.719%. In addition, significant argillaceous shedding occurs during the water–shale reaction period of 3–4 months. By testing the tensile strength, uniaxial compression decreases by 90.481% in three months. The Young's modulus of mineral points decreases to 40% after reaction for three months. The shale has softened. The softening process is nonlinear and there are inflection points. The diffusion behavior of clay minerals and the expansion behavior of new fractures are observed by CT during 3–4 months of water–shale reaction. The results show that the shale softening and pore fracture structure changes are non-linear and heterogeneous, resulting in critical water–shale reaction time. According to the experimental results, the critical water–shale reaction time can be summarized. In this time, the fracture volume increases significantly, which is conducive to increasing oil and gas production. However, the fracture volume is not significantly increased by prolonging the shut-in time. The experimental results can guide the design of hydraulic fracturing shut-in time of shale reservoirs.

Keywords: shale; water–shale reaction; pore–fracture structure; shut-in time

check for updates

Citation: Zeng, B.; Dong, E.; Yao, Z.; Song, Y.; Xiong, Z.; Huang, Y.; Gou, X.; Hu, X. Strategies for Optimizing Shut-In Time: New Insights from Shale Long-Term Hydration Experiments. *Processes* **2024**, *12*, 1096. https://doi.org/10.3390/pr12061096

Academic Editor: Carlos Sierra Fernández

Received: 9 April 2024
Revised: 8 May 2024
Accepted: 16 May 2024
Published: 27 May 2024

Copyright: © 2024 by the authors. Licensee MDPI, Basel, Switzerland. This article is an open access article distributed under the terms and conditions of the Creative Commons Attribution (CC BY) license (https://creativecommons.org/licenses/by/4.0/).

1. Introduction

Hydraulic fracturing technology is widely used in the development of shale reservoirs [1,2]. Shut-in time usually lasts for months. Since fracturing fluid enters the shale reservoir, water-sensitive minerals represented by illite combine with water molecules to produce a water–shale reaction [3–5]. The mechanical properties and pore–fracture structure of the shale reservoir change. Li et al. established a shale swelling model and analyzed the correlation between swelling and the reduction in Young's modulus [6]. Liu et al. found that shale creep is exacerbated by mineral shedding and softening in the water–shale reaction [7]. Li et al. found that sub-supercritical water reacts with shale organic matter to form nanopores [8]. Liu et al. prepared shale powder, tested saturated water and circulating water vapor, and found that the water–shale force caused by capillary force would destroy

the inner wall of nanopores during the experiment [9], improving reservoir porosity and permeability. Jin et al. found that during the water–shale reaction, the content of pyrite and organic matter decreased, accompanied by an increase in shale porosity [10,11]. In addition, many scholars have elaborated on the expansion phenomenon of clay minerals after contact with water based on XRD scanning experiments. This expansion phenomenon is explained by the change in the peak value of the XRD curve and the increase in the relative proportion of clay content [12,13]. Based on NMR scanning technology, Lin et al. found that the water–shale reaction resulted in an increase in pore volume, and in most cases, the increase in micro-pore quantity resulted in an increase in overall pore volume [14]. Li et al. made a visual and quantitative characterization of the pore structure of shale and divided the pore changes into intra-granular dissolution pores, pyrite dissolution pores, and intergranular dissolution pores according to the inducement [15]. Shao et al. found that 500–1000 nm pores were formed by mineral dissolution based on laboratory tests, which dominated the changes in pore structure [16].

Jiang et al. found that the water–shale reaction rate is gradually accelerated, that is, the soluble mineral solution will accelerate the water–shale reaction [17]. The study of Buchner et al. confirmed the increase in reaction speed and found that the reason for the increase in reaction speed was the formation of sulfate after the dissolution of pyrite, which placed the shale specimen in an acidic solution, and prolonged water–shale reaction time could reduce the liquid pH value [3,4].

In the actual production of shale reservoirs, it is common for wells to be smothered for several months. As a result, the water–shale reaction time needs to be extended. There have been many studies of water–shale reactions in shale reservoirs that occur within a few days, and a lack of studies that last several months. The mechanism of the long-term water–shale reaction is still unclear, especially the expression of the lack of water–shale reaction-induced fracture growth. In this paper, water–shale reaction experiments are carried out on surface shale outcrop specimens for 3–6 months to test shale mineral components and mechanical parameters. The fracture propagation process induced by the water–shale reaction is observed by CT scanning technology, and the changes in shale physical properties during long-term water–shale reactions are identified. The changes of mechanical properties and fracture propagation induced by long-term water–shale reactions have important guiding significance to the optimization of shut-in time in fracturing construction.

2. Materials and Methods

2.1. Experimental Material

The shale specimens used in this experimental study are all taken from a surface shale outcrop. Figure 1 shows the acquisition process of the shale specimens used in this paper.



Figure 1. Shale specimens acquisition process.

Figure 2 shows the precision cutting system used to produce block shale specimens #2, #3, and #4. All the shale specimens are not in contact with water during the processing, and after the processing is completed, they are stationary in a water-free environment at

normal temperature and pressure for one month. The above treatment method makes the shale sample close to zero water content in the initial stage of the water–shale reaction.

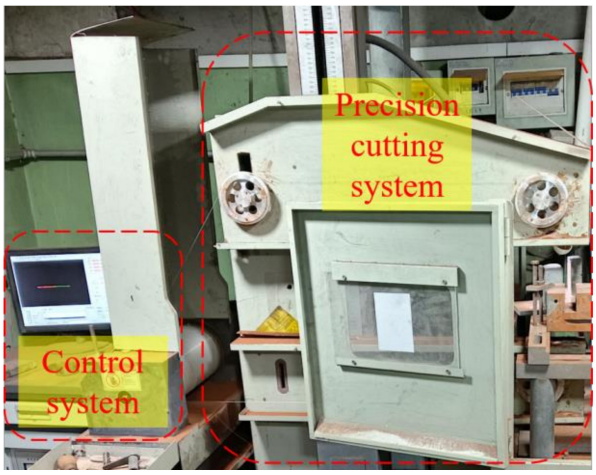

Figure 2. Precision cutting system.

The porosity and permeability of typical shale specimens are tested by nitrogen. Figure 3 shows the shale porosity and permeability test system used in this article. The average porosity and permeability of shale specimens are 3.09%, 0.01 mD, Young's modulus is 20.437 MPa, and Poisson's ratio is 0.290.

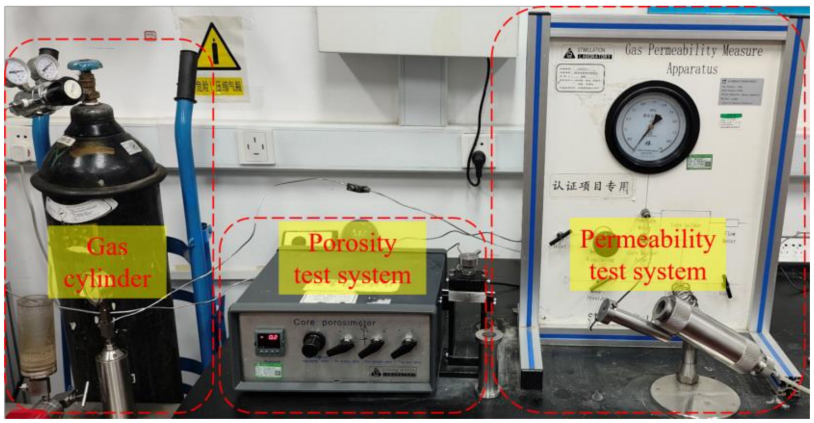

Figure 3. Shale porosity and permeability test system.

According to the needs of the experiment, the specimens are cut into #1, #2, #3, and #4, respectively. Among them, the #1 rock sample is prepared by the repeated process of grinding, sieve analysis, and grinding, so that the particle size of the rock powder is between 200–400 mesh. Size #2–#4 rock samples are made to preset dimensions by precision wire cutting method. Specimen size, quantity, and experimental use are shown in Table 1. All the specimens are immersed in pure water, and the long-term water–shale reaction is carried out for 3–6 months, respectively, to simulate the reservoir shale smothering process. Test and observe shale mechanical properties, mineral morphology, and natural fracture growth.

Table 1. Specimen preparation parameters and experimental use.

Serial Number	Specimen Size	Quantity	Application	Parameter	Typical Specimen
#1	200–400 mesh powder	1000 g	XRD Scan	Scanning Angle 3.5° to 45°	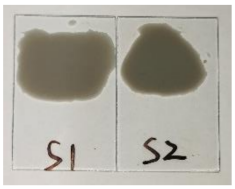
#2	ϕ25 mm ×5 mm	2	Nanoindentation	Depth 3000 nm	
#3	ϕ25 mm ×10 mm	4	Uniaxial compression	Uniaxial loading to specimen rupture	
#4	ϕ25 mm ×50 mm	6	CT Scan	Layer thickness 0.625 mm, Voltage 120 mV, Electric current 140 mA	

Figure 4a,b shows the water–shale reaction vessel used in this paper. On the left in Figure 4a, size #1 rock powder is immersed in a 500 mL beaker filled with water, and on the right in Figure 4b, a massive rock sample is immersed in 100 mL pure water. The containers are sealed and kept at normal temperature and pressure.

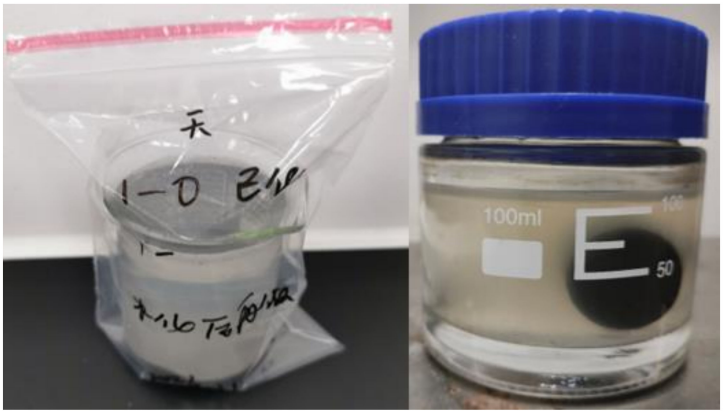

(**a**) (**b**)

Figure 4. (**a**,**b**) Water–shale reaction vessel.

2.2. Experimental Method

XRD test method: The pattern is ground into powder and placed on the glass sheet to scan and measure the mineral composition and mass fraction of the shale specimen. When testing the clay composition, the shale powder should be immersed in distilled water, and after standing for 3 h, the upper 3.75 cm suspension should be extracted with a syringe for centrifugation to obtain the clay specimen to be tested. The samples are made into natural specimens, ethylene glycol-saturated specimens, and high-temperature specimens for scanning. The scanning speed is 3°/min, and the scanning range is 3.5°–15°/3.5°–30°/3.5°–15°. The above three specimens are three test stages of the same specimen, so they cannot be reused. Then, Rockquan 2020 and Clayquan 2016 professional mineral

and clay composition analysis software are used for quantitative analysis. The test results are processed in strict accordance with the oil industry standards SY/T5163-2010 [18] (quantitative calculation) and SY/T 5477-2003 [19] (mixed-layer ratio calculation). Figure 5 shows the XRD curve measured by shale powder #1-S1. Figure 5a shows the mineral spectrum of shale powder, and Figure 5b shows the shale powder. XRD test can find the change in clay and mineral content during the long-term water–shale reaction. This helps to clarify the long-term water–shale reaction mechanism and provides support for the results of subsequent shale mechanical tests and CT scans.

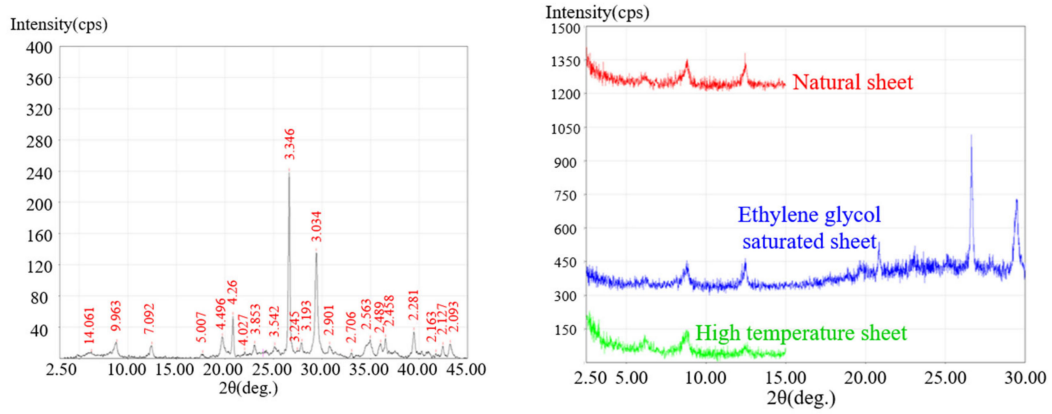

Figure 5. XRD test results of #1-S1 shale specimen: (**a**) mineral spectrum; (**b**) clay spectrum.

Nanoindentation experiment method: The quasi-static nanoindentation method is selected, the tip indenter is pressed into the surface of the specimen at a strain rate of 0.05 s^{-1}, the surface of the specimen is elastoplastic deformation, and after reaching the maximum load, the load and unloading process is unloaded at a certain rate to obtain the load–displacement curve, which can be used to calculate Young's modulus and hardness of the shale. Figure 6 shows the standard stress load–displacement curve of the nanoindentation experiment. Figure 7 shows the size parameters of the loading tip pressed into the shale surface. Young's modulus and surface hardness of shale can be measured by nanoindentation experiment without significant damage to shale specimens. It is helpful to clarify the changes in rock mechanics in the long-term water–shale reaction.

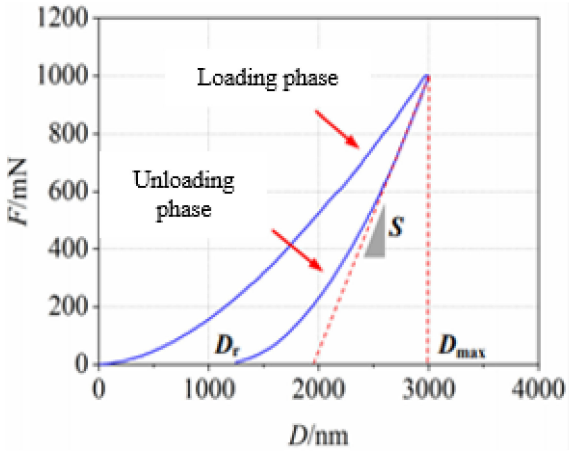

Figure 6. Typical stress load–displacement curve for nanoindentation experiments.

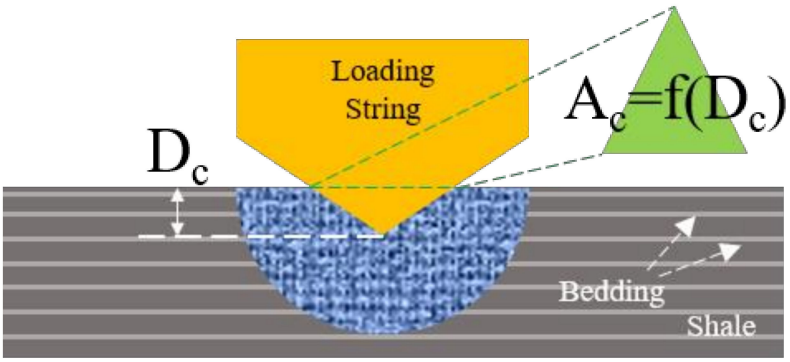

Figure 7. Schematic diagram of indenter pressing depth and deformation area.

The calculation principle of Young's modulus and surface hardness of the specimen are shown in Equations (1)–(3) [20,21]. The Young's modulus described in this paper is a reduced Young's modulus E_r which can be directly measured.

$$H = \frac{P}{A_c} \tag{1}$$

$$E_r = \frac{S\sqrt{\pi}}{2\sqrt{A_c}} \tag{2}$$

$$\frac{1}{E_r} = \frac{1-\nu^2}{E} + \frac{1-\nu_i{}^2}{E_i} \tag{3}$$

In the above formula, H is the surface hardness of the specimen; P is for load; Ac represents the contact area projection; E_r is for reduced elastic modulus; S is the slope of the unloading curve; E_i is Young's modulus and Poisson's ratio of the indenter, and E is Young's modulus and Poisson's ratio of the specimen, respectively.

The test method of tensile strength: Figure 8a,b show the schematic diagram of the shale tensile strength test method. The vertical cylindrical axis of the shale specimen in the direction of shale bedding is selected for the experiment to reduce the influence of beddings on the tensile strength of shale. The load data are recorded in real time during the loading process of the indenter, and the tensile strength of the shale is calculated according to the load when the shale specimen breaks. The calculation method is shown in Equation (4).

$$\sigma_t = \frac{2F}{\pi Dh} \tag{4}$$

where σ_t is tensile strength, MPa; F is load, N; D is the diameter of the shale specimen, mm; h is the thickness of the shale specimen, mm.

The test method of CT scan: The specimens are scanned immediately after the water–shale reaction. CT images are obtained through CT post-processing, and the morphology and volume changes of fracture bodies in shale specimens are compared and observed. The pore–fracture volumes are calculated. The fractures can be visually distinguished by the staining method. CT number is a function of the density of scanned shale specimens, which can directly reflect the morphology of pores and fractures inside shale specimens [22]. CT image post-processing involves parameter setting and other operations, all of which can be seen in Table 2.

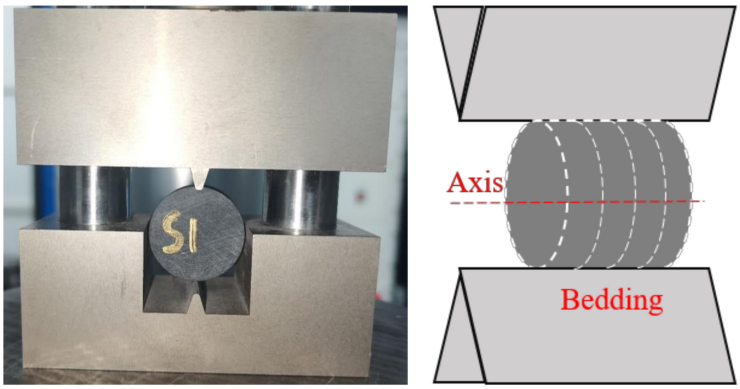

(**a**) (**b**)

Figure 8. (**a**,**b**) Tensile strength test picture and shale bedding direction diagram.

Table 2. CT post-processing parameters.

Parameters	Values
Intensity Range	50–1000
Filter-Volume3d	>50 mm^3

3. Results and Discussion

3.1. Testing of Shale Mineral Components Based on XRD Scanning

Figure 9 shows that the initial XRD scanning experiment shows that quartz, calcite, and clay minerals are the main components of the shale specimens. Among them, quartz and calcite mainly have brittle mechanical characteristics are relatively stable in water and are less affected by water–shale reaction time. The average content of clay minerals is the highest with 34.7 wt%. The clay minerals are mainly composed of illite and chlorite, in which illite is the main component and has a strong water–shale reaction and expansion characteristics [3]. This provides a material basis for the follow-up experiment to observe the variation of shale specimens during the water–shale reaction.

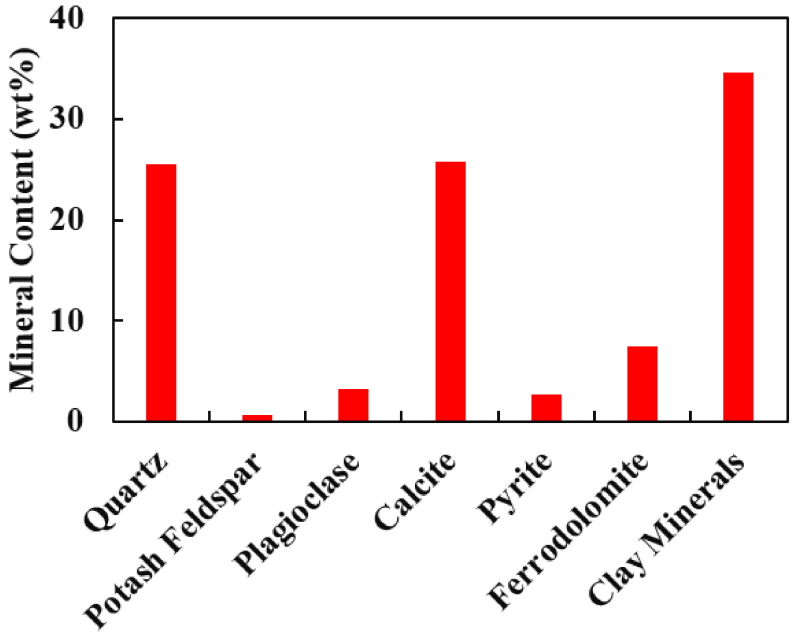

Figure 9. Average mass fraction of each component of shale specimen.

During the water–shale reaction process of the shale specimen, four XRD scanning experiments are conducted one month apart. As shown in Figure 10a, the overall mass fraction of clay minerals increases from 34.7% to 39.8% during the water–shale reaction process. However, because the experimental method described in Section 2.2 cannot be repeated, the test results fluctuate. The specimens contain only two types of clay, illite and chlorite. These two clay molecular structures determine that illite easily absorbs water and expands, while chlorite is relatively stable [23,24]. Based on the stability of chlorite in the water–shale reaction, it can be considered that the total amount of chlorite is unchanged. It is inferred that the increase in the total amount of clay is caused by the expansion of illite. The comparison results of the relative contents of illite and chlorite in the clay can be seen in Figure 10b. The relative mass fraction of illite increases from 70% to 80.5% in the process of water absorption and expansion. In this process, the increase rate is faster from before the water–shale reaction to one month, and then the content is stable. This results in a corresponding decrease in the mass fraction of weakly absorbent chlorite.

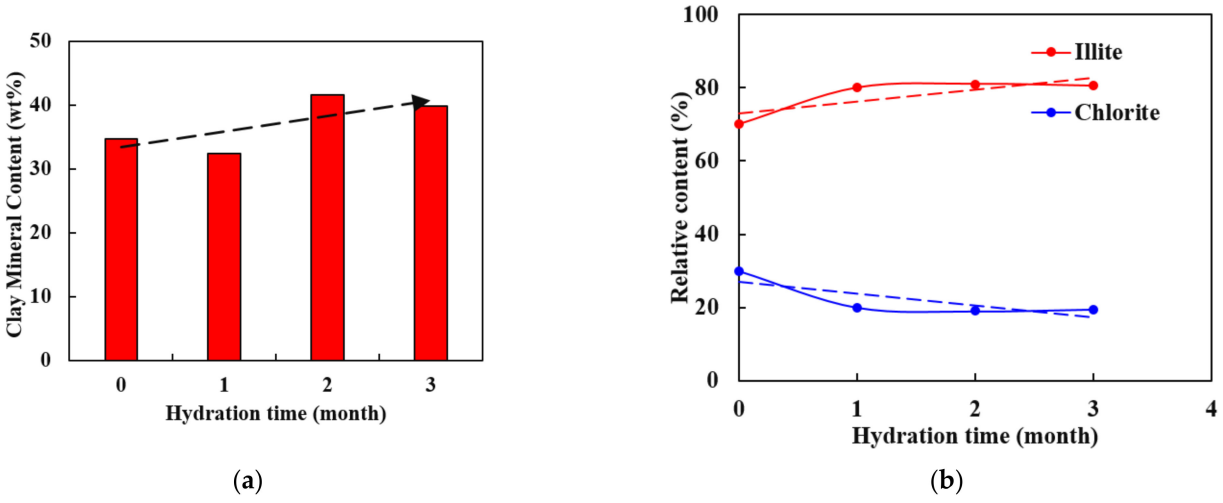

(**a**) (**b**)

Figure 10. Change of clay content with water–shale reaction time (**a**): change of clay mass fraction; (**b**): clay composition mass fraction change).

3.2. Shale Tensile Strength Test Based on Uniaxial Compression Experiment

The tensile strength of the shale is tested by uniaxial compression, which causes the shale specimen to fracture. When cutting the cylindrical shale specimen, set the shale specimen axis direction perpendicular to the bedding to reduce the influence of bedding on experimental results. Figure 11 shows the test results of shale tensile strength. The tensile strength of shale specimens decreases from 5.5 MPa to 0.53 MPa during 3 months of water–shale reaction. The reduction is 90.36%. This indicates that in the long-term water–shale reaction, shale pore initiation, connectivity, and fracture expansion significantly reduce the tensile strength. In the process of hydraulic fracturing, increasing the duration of drilling is conducive to reducing shale fracture pressure and facilitating microfracture expansion.

The mechanism of the decrease in tensile strength is speculated. In the process of a long-term water–shale reaction, water molecules fill the crystal layers of water-absorbing and expansive minerals represented by illite, and the mineral strength decreases while the volume expands [25–27]. The volume expansion of minerals produces tensile stress, which acts on the surrounding matrix. Combine with soluble mineral corrosion to initiate micro-fractures. Micro-fracture initiation is discussed in detail in Section 3.4 CT scan results.

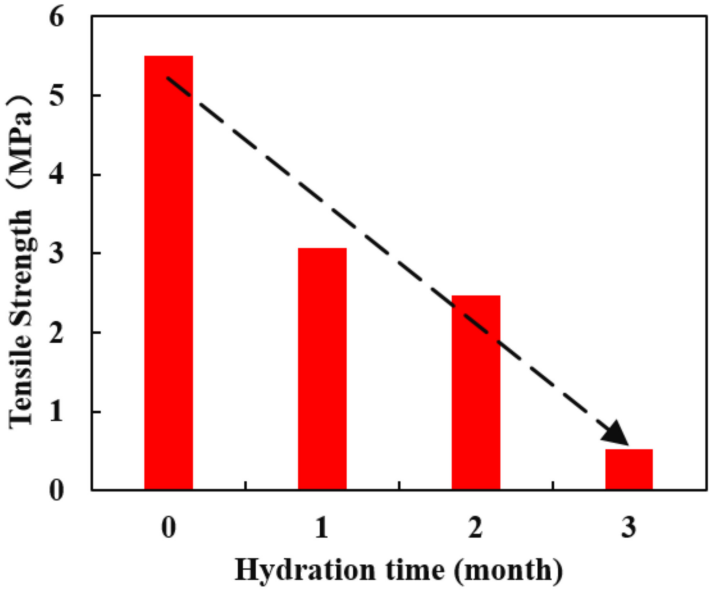

Figure 11. Test results of shale tensile strength.

3.3. Mechanical Parameter Testing Based on Nanoindentation

The changes in Young's modulus and Poisson's ratio of shale specimens during the long-term water–shale reaction are measured by the nanoindentation experiment. Figure 12 shows that light yellow mineral points are visible on the surface of the test shale specimen and the test points are divided into mineral points and matrix points.

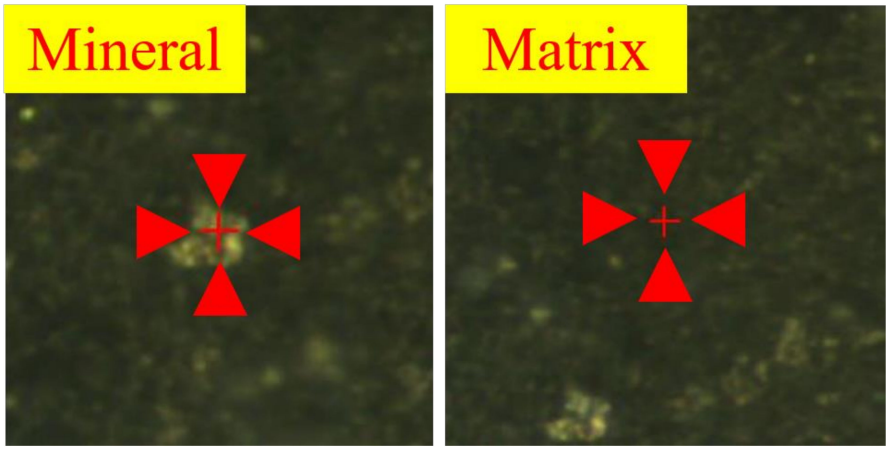

Figure 12. Schematic diagram of test points.

According to the loading and unloading process of the test indenter pressed into the surface of the shale specimen during the experiment, parameters such as the pressing depth and load are recorded, and Young's modulus and surface hardness of the measuring points are calculated by substituting them into Equations (1) and (2). Figure 13 shows the results of the shale nanoindentation experiment. The surface hardness test results of shale matrix points and mineral points do not show a significant trend, and these test results are affected by the heterogeneity of the shale matrix. On the contrary, Young's model of mineral measurement points showed a steady decline trend. Based on the theory of molecular dynamics, the research results of the clay mineral water–shale reaction mechanical damage model established by predecessors are confirmed by this experiment [25]. When water molecules enter the illite interlayer, the effect of interlayer force is weakened, and the elasticity of the shale specimen is weakened, that is, Young's modulus is decreased.

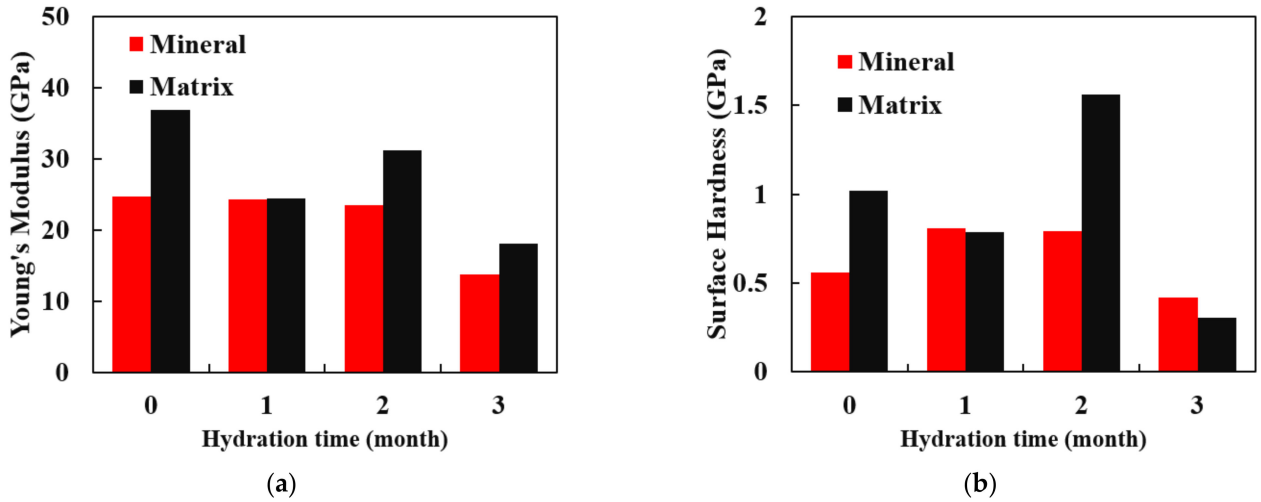

Figure 13. Results of nanoindentation experiment: (**a**) Young's modulus at measuring point; (**b**) surface hardness at measuring point.

It is worth noting that all the experiments in Sections 3.1–3.3 are affected by experimental methods and sampling locations, and it is difficult to repeat experiments on the same shale specimen and avoid the impact of shale heterogeneity. Subsequently, non-destructive experiments are carried out to determine the structural changes of the same shale specimen during the long-term water–shale reaction. It also helps to verify the inference of micro-fracture propagation in Section 3.2.

3.4. CT Scan

CT scan is used to observe the fracture morphology and calculate the fracture volume during the process of the water–shale reaction. Table 3 CT images of the shale matrix are shown in Figure (A). The edges of the orange-red high-density mineral area are clear with strong interlayer differences. According to the XRD results in Section 3.1, the shale specimens mainly contain quartz, calcite, illite, and chlorite, and their densities are generally 2.5–2.6 g/cm^3, while only illite density ranges from 2.7–2.9 g/cm^3. It is inferred that the red areas in the image represent the illite-rich area, which is marked as the five major rich areas a–e in (A) in Table 3. The illite in the shale specimen falls off and shifts after the water–shale reaction expansion [28], and finally adheres to the outer surface of the shale specimen. This causes the outer surface of the shale specimen shown in 4(A)–6(A) in Table 3 to be highlighted. The three figures (A), (B), and (C) in Table 3 all correspond to the same angle of the same shale specimen. The water–shale reaction-induced fracture initiation and expansion process is revealed through the increase or decrease of fracture volume and morphological changes by color-marking and differentiating fractures or pore throat connections larger than 50 mm^3.

From 1 to 2 months of water–shale reaction, illite hydration expands at positions a and b, resulting in fracture body No. 1 and No. 2 connecting discrete pores, and fracture volume increases by 42.0% and 54.9%, respectively. The water–shale reaction at the c position leads to a significant increase in discrete pores. In addition, obvious fracture propagation is observed at fracture No. 4, and the fracture morphology expands from semicircular to nearly circular. The volume increases from 81.4 mm^3 to 234.8 mm^3, an increase of 188.5%. However, there is no obvious illite enrichment area here, and the fracture propagation is dominated by corrosion [17,29]. The expansion of the above fractures compresses fractures 3, 5, and 6, resulting in volume reduction. Fracture No. 6 has the most significant morphological changes, with partial closure and volume reduction of 61.4%. Overall, the fracture volume increases by 6.9% from 1585.4 mm^3 to 1694.7 mm^3.

Table 3. CT shale specimen-fracture body image.

Serial Number	(A) Matrix Scanning	(B) Matrix–Fracture Contrasting	(C) Fracture Volume Segmentation
#1	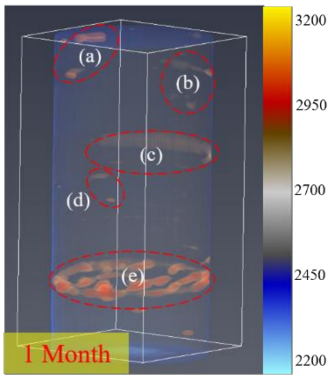	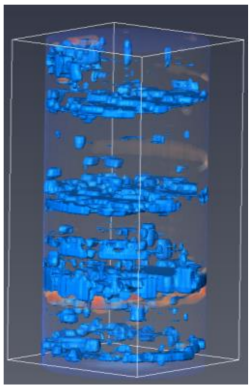	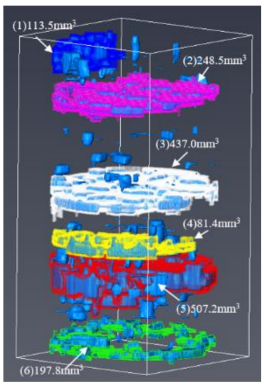
#2	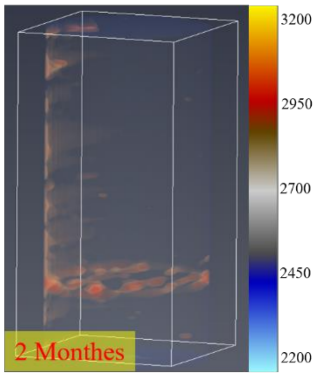	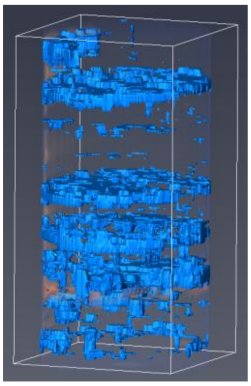	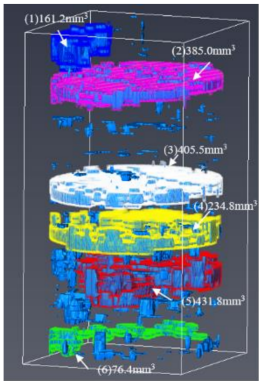
#3	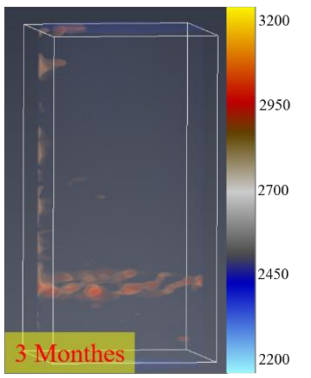		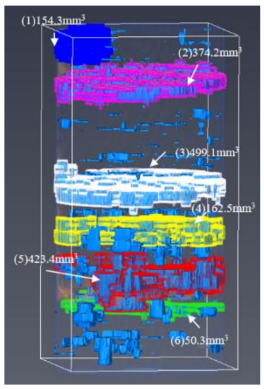
#4	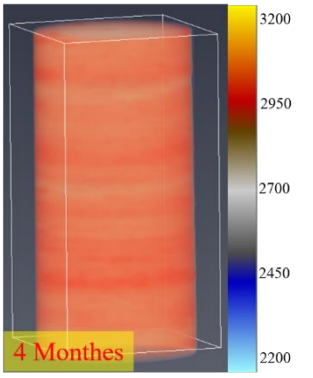	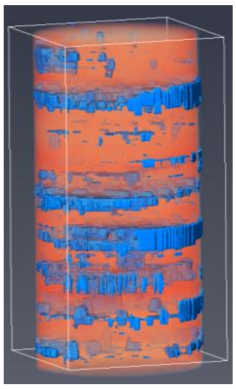	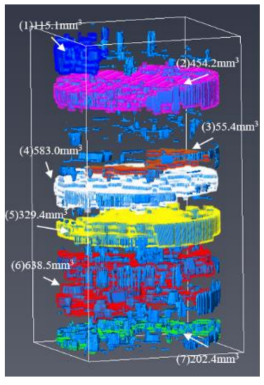

Table 3. *Cont.*

Serial Number	(A) Matrix Scanning	(B) Matrix–Fracture Contrasting	(C) Fracture Volume Segmentation
#5	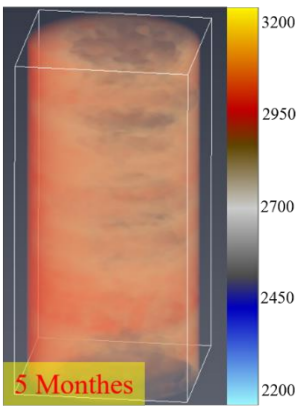		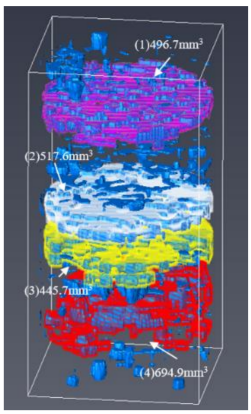
#6	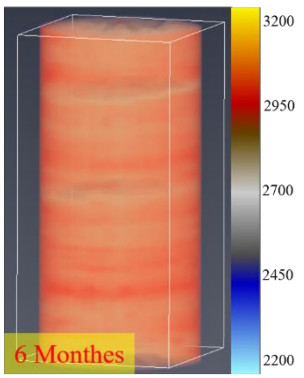	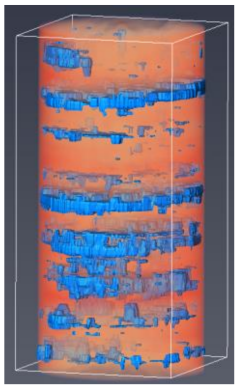	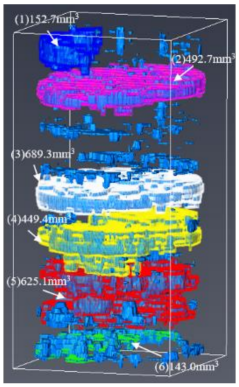

The water–shale reaction from 2 to 3 months, illite in areas a, b, and c exhausted, and the discrete pores at corresponding positions stop expanding. The hydration of illite in region D led to the connection of discrete pores in fracture No. 3, and the volume increases from 405.5 mm^3 to 499.1 mm^3, with an increase of 23.1%. The discrete pores of the original fracture 5–6 are connected to form a new fracture, squeezing the original fracture, resulting in the squeezing of fracture 6. This process of competitive expansion of the fracture is shown as the displacement of the green fracture in the image.

During the water–shale reaction, the most obvious increase in fracture volume occurred from 3 to 4 months, with the fracture volume increasing from 1663.7 mm^3 to 2378.0 mm^3, an increase of 42.9%, which also indicates that a severe water–shale reaction occurred during this period. In addition, compared with CT images of 3(C) and 4(C), it can be found that the discrete pores are significantly increased, the connectivity between pores and fractures is enhanced, and fractures No. 5 and 6 in 3(C) are connected and merged to form fractures No. 6 in 4(C) with a larger volume. The merging process of these two fractures alone generates a new fracture space of 164.8 mm^3. For shale oil and gas reservoirs with natural fracture development, the target of reservoir reconstruction is to expand the reconstruction volume. Increasing the number of main fracture communication pores and natural fractures is conducive to the exploitation of oil and gas enrichment in the pores and natural fractures. This kind of sudden increase in fracture volume has important guiding significance for the boring process. If the shut-in time exceeds this stage, the fracturing reconstruction volume will be effectively increased, which will help to increase the oil and gas production of the shale reservoir.

The water–shale reaction time is between 4 and 5 months due to fracture-to-fracture interference and possible blockage during the mineral shedding process, and the fracture volume decreases. After 5–6 months of water–shale reaction, the fracture volume increases

again and is slightly higher than the fracture volume at 4 months of water–shale reaction. Table 4 and Figure 14 show each fracture volume and total volume. Obviously, the fracture volume increases significantly during the water–shale reaction period of 3 to 4 months. Based on the induced fracture volume surge during 3–4 months of the water–shale reaction, it can be determined that the water–shale reaction reaches a critical value during 3–4 months. Stopping shut-in and starting the product at this time will help increase oil and gas recovery efficiency. The growth of fracture volume will be limited if the shut-in time is prolonged. Therefore, extending the period of shut-in time after four months will not increase oil and gas production, but will delay oil and gas production time, which is not conducive to enhanced oil recovery.

Table 4. Fracture volume.

Water–Shale Reaction Time (Months)	Fracture Serial Number	1	2	3	4	5	6
Fracture volume (mm^3)	(1)	113.533	161.213	50.3182	115.117	496.714	152.688
	(2)	248.489	384.983	423.42	454.160	517.588	492.693
	(3)	437.014	405.483	162.469	55.416	445.671	689.304
	(4)	81.365	234.800	499.051	583.010	694.907	449.363
	(5)	507.217	431.763	374.157	329.376	——	625.078
	(6)	197.798	76.421	154.317	638.536	——	143.042
	(7)	——	——	——	202.372	——	——
Total volume (mm^3)		1585.416	1694.663	1663.732	2377.987	2154.88	2552.168

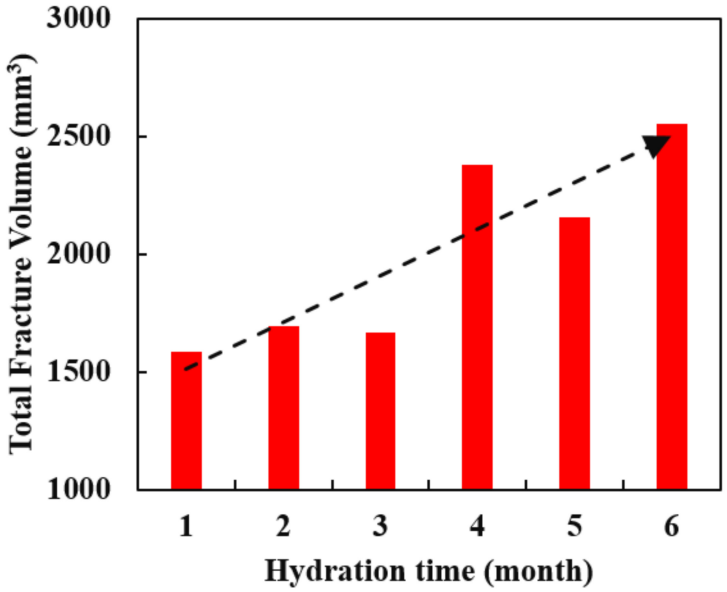

Figure 14. Total fracture volume scanned by CT.

4. Conclusions

1. After three months of the water–shale reaction, the overall mass fraction of clay minerals increases from 34.7% to 39.8%, and the proportion of illite increases from 70% to 80.5%, with an upward trend showing a steep rise at first and then a stable trend.
2. The uniaxial compression experiment shows that the tensile strength of the shale specimens decreases significantly by 90.36% in the first three months of the water–shale reaction, indicating that shale pore initiation, connectivity, and fracture expansion significantly reduce the tensile strength. After hydraulic fracturing, prolonging the shut-in time is conducive to reducing shale fracture pressure and promoting microfracture propagation.

3. The nanoindentation experiment shows that in the first three months of the water–shale reaction, the mineral point Young's modulus decreases, marking the mineral softening.
4. The process of fracture expansion is carefully observed by the CT scanning experiment. Based on the phenomenon of abrupt increases in fracture volume, the critical shut-in time is anchored at four months. The fractures that expand under the influence of the water–shale reaction communicate the discrete pores and natural fractures of oil and gas enrichment, contributing to enhanced oil recovery. This indicates that the shut-in time of 4 months helps to expand the fracture space and increase the recovery. However, after 4 months of shut-in time, adding more time will not contribute much to the stimulation.

Author Contributions: Investigation, B.Z., Z.Y., Y.S., Y.H. and X.G.; Resources, B.Z., Z.Y., Y.S. and Y.H.; Data curation, Z.X. and X.G.; Writing—original draft, E.D.; Writing—review & editing, X.H. All authors have read and agreed to the published version of the manuscript.

Funding: This research received financial support from the China University of Petroleum (Beijing) School for Young Talent Startup Fund (No. ZX20190183).

Data Availability Statement: The data presented in this study are available on request from the corresponding author.

Acknowledgments: The author is especially grateful to Professor Fujian Zhou for providing experimental instrument support.

Conflicts of Interest: Authors: Bo Zeng, Zhiguang Yao, Yi Song, and Yongzhi Huang are employed by the PetroChina Southwest Oil & Gasfield Company; the remaining authors declare that the research was conducted in the absence of any commercial or financial relationships that could be construed as a potential conflict of interest.

References

1. Zou, C.; Dong, D.; Wang, Y.; Li, X.; Huang, J.; Wang, S.; Guan, Q.; Zhang, C.; Wang, H.; Liu, H.; et al. Shale gas in China: Characteristics, challenges and prospects (II). *Pet. Explor. Dev.* **2016**, *43*, 182–196. [CrossRef]
2. Melikoglu, M. Shale gas: Analysis of its role in the global energy market. *Renew. Sustain. Energy Rev.* **2014**, *37*, 460–468. [CrossRef]
3. Buchner, T.; Kiefer, T.; Zelaya-Lainez, L.; Gaggl, W.; Konegger, T.; Füssl, J. A multitechnique, quantitative characterization of the pore space of fired bricks made of five clayey raw materials used in European brick industry. *Appl. Clay Sci.* **2021**, *200*, 105884. [CrossRef]
4. Feng, J.; Tian, H.; Huang, Y.; Ding, Z.; Yin, Z. Pyrite oxidation mechanism in aqueous medium. *J. Chin. Chem. Soc.* **2019**, *66*, 345–354. [CrossRef]
5. Fathy, D.; Wagreich, M.; Fathi, E.; Ahmed, M.S.; Leila, M.; Sami, M. Maastrichtian Anoxia and Its Influence on Organic Matter and Trace Metal Patterns in the Southern Tethys Realm of Egypt during Greenhouse Variability. *ACS Omega* **2023**, *8*, 19603–19612. [CrossRef] [PubMed]
6. Li, Z.; Li, G.; Li, H.; Liu, J.; Jiang, Z.; Zeng, F. Effects of shale swelling on shale mechanics during shale–liquid interaction. *Energy* **2023**, *279*, 128098. [CrossRef]
7. Liu, Y.; Yang, C.; Wang, J.; Xiong, Y.; Peng, P. New insights into hydration-induced creep behavior of shale: A comparison study of brittle black shale and clayey oil shale at micro-scale. *Mar. Pet. Geol.* **2022**, *138*, 105554. [CrossRef]
8. Li, C.; Jin, Z.; Zhang, L.; Liang, X. Advancing the application of sub- and supercritical water in the in-situ conversion of immature and low-maturity shale. *Fuel* **2024**, *359*, 129891. [CrossRef]
9. Liu, A.; Liu, S.; Zhang, R.; Sang, G.; Xia, K. Cyclical water vapor sorption-induced structural alterations of mine roof shale. *Int. J. Coal Geol.* **2023**, *273*, 104267. [CrossRef]
10. Jin, L.; Rother, G.; Cole, D.R.; Mildner, D.F.; Duffy, C.J.; Brantley, S.L. Characterization of deep weathering and nanoporosity development in shale—A neutron study. *Am. Miner.* **2011**, *96*, 498–512. [CrossRef]
11. Fathy, D.; Baniasad, A.; Littke, R.; Sami, M. Tracing the geochemical imprints of Maastrichtian black shales in southern Tethys, Egypt: Assessing hydrocarbon source potential and environmental signatures. *Int. J. Coal Geol.* **2024**, *283*, 104457. [CrossRef]
12. Chavali, R.V.P.; Vindula, S.K.; Reddy, P.H.R.; Babu, A.; Pillai, R.J. Swelling behavior of kaolinitic clays contaminated with alkali solutions: A micro-level study. *Appl. Clay Sci.* **2017**, *135*, 575–582. [CrossRef]
13. Amorim, C.L.G.; Lopes, R.T.; Barroso, R.C.; Queiroz, J.C.; Alves, D.B.; Perez, C.A.; Schelin, H.R. Effect of clay–water interactions on clay swelling by X-ray diffraction. Nuclear Instruments and Methods in Physics Research Section A: Accelerators, Spectrometers, Detectors and Associated. *Equipment* **2007**, *580*, 768–770.
14. Lin, H.; Sun, X.; Yuan, Y.; Lai, X.; Qu, H.; Luo, C. Experimental investigation on the dynamic volume changes of varied-size pores during shale hydration. *J. Nat. Gas Sci. Eng.* **2022**, *101*, 104506. [CrossRef]

15. Li, N.; Jin, Z.; Zhang, S.; Wang, H.; Yang, P.; Zou, Y.; Zhou, T. Micro-mechanical properties of shale due to water/supercritical carbon dioxide-rock interaction. *Pet. Explor. Dev.* **2023**, *50*, 1001–1012. [CrossRef]
16. Shao, J.; You, L.; Jia, N.; Kang, Y.; Chen, M. Investigation of induced change in pore structure by the reaction of shale with fracturing fluid. *Gas Sci. Eng.* **2023**, *110*, 204860. [CrossRef]
17. Jiang, L.; Zhou, H.; Peng, X. Bio-oxidation of pyrite, chalcopyrite and pyrrhotite by Acidithiobacillus ferrooxidans. *Chin. Sci. Bull.* **2007**, *52*, 2702–2714. [CrossRef]
18. *SY/T5163-2010*; Analysis Method for Clay Minerals and Ordinary Non-Clay Minerals in Sedimentary Rocks by the X-ray Diffraction. National Energy Administration: Beijing, China, 2010.
19. *SY/T 5477-2003*; The Division of Diagenetic Srages in Clastic Rocks. State Economic and Trade Commission: Beijing, China, 2003.
20. Oliver, W.C.; Pharr, G.M. Measurement of hardness and elastic modulus by instrumented indentation: Advances in understanding and refinements to methodology. *J. Mater. Res.* **2004**, *19*, 3–20. [CrossRef]
21. Oliver, W.C.; Pharr, G.M. An improved technique for determining hardness and elastic modulus using load and dis-placement sensing indentation experiments. *J. Mater. Res.* **1992**, *7*, 1564–1583. [CrossRef]
22. Martinez-Angeles, R.; Hernandez-Escobedo, L.; Perez-Rosales, C. 3 D Quantification of Vugs and Fractures Networks in Limestone Cores. In Proceedings of the SPE Annual Technical Conference and Exhibition, Houston, TX, USA, 3–5 October 2022.
23. Grim, R.E. Clay Mineralogy. *Soil Sci.* **1953**, *76*, 317. [CrossRef]
24. Tournassat, C.; Steefel, C.I.; Bourg, I.C.; Bergaya, F. *Natural and Engineered Clay Barriers*; Elsevier: Amsterdam, The Netherlands, 2015.
25. Carrier, B.; Vandamme, M.; Pellenq, R.J.-M.; Van Damme, H. Elastic Properties of Swelling Clay Particles at Finite Temperature upon Hydration. *J. Phys. Chem. C* **2014**, *118*, 8933–8943. [CrossRef]
26. Carrier, B.; Vandamme, M.; Pellenq, R.J.-M.; Bornert, M.; Ferrage, E.; Hubert, F.; Van Damme, H. Effect of Water on Elastic and Creep Properties of Self-Standing Clay Films. *Langmuir* **2016**, *32*, 1370–1379. [CrossRef] [PubMed]
27. Zhang, L.; Lu, X.; Liu, X.; Yang, K.; Zhou, H. Surface Wettability of Basal Surfaces of Clay Minerals: Insights from Molecular Dynamics Simulation. *Energy Fuels* **2016**, *30*, 149–160. [CrossRef]
28. Li, Q.; Li, J.; Zhu, B. Experimental investigation of the influence of sequential water-rock reactions on the mineral altera-tions and porosity evolution of shale. *Constr. Build. Mater.* **2022**, *317*, 125859. [CrossRef]
29. Liao, X.; Chigira, M.; Matsushi, Y.; Wu, X. Investigation of water–rock interactions in Cambrian black shale via a flow-through experiment. *Appl. Geochem.* **2014**, *51*, 65–78. [CrossRef]

Disclaimer/Publisher's Note: The statements, opinions and data contained in all publications are solely those of the individual author(s) and contributor(s) and not of MDPI and/or the editor(s). MDPI and/or the editor(s) disclaim responsibility for any injury to people or property resulting from any ideas, methods, instructions or products referred to in the content.